INORGANIC CHEMISTRY FRONTIERS

RESEARCH ARTICLE

View Article Online
View Journal | View Issue

Cite this: *Inorg. Chem. Front.*, 2023, **10**, 3383

Lanthanide-doped lead-free double perovskite La_2MgTiO_6 as ultra-bright multicolour LEDs and novel self-calibrating partition optical thermometer†

Keming Zhu, Hanyu Xu, Zhiying Wang and Zuoling Fu *

The infinite potential of lanthanide in optoelectronic research has triggered the search for ideal host materials. Herein, based on the excellent lanthanide compatibility of double perovskite La_2MgTiO_6, light-responsive multifunctional phosphors with four modes were successfully constructed (Modes I–IV: Tm–Yb; Er–Yb; Ho–Yb; Er/Tm–Yb). After systematically exploring the internal mechanism of high-purity and brightness upconversion (UC) photoluminescence behind the four modes, intense green, blue and near-white lighting-emitting diodes (LEDs) were fabricated. Besides, aiming at the different emission energy levels of the monitored bands, the temperature-sensing performance of Modes I–IV was strictly evaluated utilizing thermally coupled or non-thermally-coupled luminescence intensity ratio (LIR) techniques. All the modes demonstrate excellent temperature measurement potential, stability and repeatability. Especially in Mode IV, a novel self-calibrating partition thermometer with dual-emitting centers originating from Er/Tm was designed successfully, which can provide specific LIR for three regions of low temperature, medium temperature and high temperature, and finally achieve high relative sensitivity over an ultra-wide temperature range. The results testify that the as-synthesized multifunctional phosphors break through the limitation of lanthanide doping types in a single material, which can realize the diversification of application functions and launch a new chapter for the design of advanced multifunctional materials.

Received 21st March 2023,
Accepted 28th April 2023

DOI: 10.1039/d3qi00529a

rsc.li/frontiers-inorganic

1. Introduction

Lanthanides (Ln^{3+}), with their rich energy level structure and excellent optical properties, have been making a splash in the fields of bioimaging, multicolour display, non-contact optical temperature detection and information storage.[1–6] Among them, with the continuous development of science and technology, the requirements for the basic but indispensable parameter of temperature are becoming more and more stringent. Therefore, the emergence of various novel non-contact temperature detection techniques has gradually replaced the traditional contact temperature measurement.[7–11] Among these, the Ln^{3+}-based luminescence intensity ratio (LIR) non-contact temperature measurement technology stands out by virtue of its fast response time, avoidance of fluorescence loss and excitation light source fluctuations, *etc.*[12] For example, Ran *et al.* used prepared $NaLaMgWO_6$:Er^{3+} phosphors to construct an optical thermometer with a relative sensitivity of 1.04% K^{-1}, which is based on the emission intensity ratio of Er^{3+} ions with thermally coupled levels (TCLs: $^2H_{11/2}/^4S_{3/2}$) at different temperatures;[13] Wu *et al.* achieved ultra-high sensitivity temperature measurement at 3.18% K^{-1} based on non-thermally-coupled levels (non-TCLs) and LIR technology using the prepared $Li_4SrCa(SiO_4)_2$:Eu^{2+} phosphors.[14] Although the above optical thermometer modes constructed by these reports show excellent sensitivity, their peaks are usually established in a narrow temperature range. This range is difficult to meet within the needs of daily life or industrial manufacturing, which hinders future commercialization, so it is urgent to design and develop fluorescent materials with excellent sensitivity in an ultra-wide temperature range.

Based on previous research, the selection of Ln^{3+} in upconversion (UC) luminescent materials is generally by $Tm^{3+}/Er^{3+}/Ho^{3+}$–Yb^{3+} doping combination.[15–17] Therefore, the appropriate host material becomes key to the success of the research.

Coherent Light and Atomic and Molecular Spectroscopy Laboratory, Key Laboratory of Physics and Technology for Advanced Batteries, College of Physics, Jilin University, Changchun 130012, China. E-mail: zlfu@jlu.edu.cn

† Electronic supplementary information (ESI) available. See DOI: https://doi.org/10.1039/d3qi00529a

Generally speaking, the choices for host material in UC luminescent materials are mainly oxide and fluoride, and there are a few quantum dot materials.[18] Among the oxide hosts, represented by Gd_2O_3 and La_2O_3, although the material itself has excellent thermal stability and environmental friendliness, the phonon energy of oxide is high.[19,20] Following the band gap law, high phonon energy will substantially reduce the UC luminous efficiency. On the other hand, fluoride (*i.e.*, $NaYF_4$, $NaGdF_4$, YF_3, LuF_3) can make up for the former high phonon energy shortcomings, but has complex preparation process, and its thermal stability is poor.[21–25] Therefore, finding perfect host materials and providing a suitable crystal field environment for all the above Ln^{3+} combinations can greatly improve the utilization rate of the materials. However, it is obviously a very challenging study.

Inspired by these, the double perovskite La_2MgTiO_6 (LMTO) was selected as an ideal host material with its excellent stability and low phonon energy in this work. On this basis, four systems of Ln^{3+} (Tm^{3+}; Er^{3+}; Ho^{3+}; Tm^{3+}/Er^{3+})-Yb^{3+} co-doped LMTO phosphors were synthesized by a simple high-temperature solid-state reaction. Due to their excellent UC photoluminescence properties, the packaged green/blue/near-white LEDs devices also exhibit outstanding performance. It is well known that materials with excellent luminescent properties can be used to make more efficient optical thermometers that can better avoid the interference of the external environment. Following this line of thinking, four different thermometer modes were established based on the above four doping systems (Fig. 1). Modes I–III, which utilize the LIR technology of TCLs (Er^{3+}) and non-TCLs (Tm^{3+} and Ho^{3+}), respectively, show ultra-high sensitivity. Especially in Mode IV, we successfully selected five independent excitation wavelengths as detection signals, combining TCLs and non-TCLs of LIR technology, and designed an accurate self-calibrating thermometer mode over a wide temperature range. All the results suggest that the as-synthesized Ln^{3+} (Tm^{3+}, Er^{3+}, Ho^{3+}, Tm^{3+}/Er^{3+})-Yb^{3+} co-doped LMTO phosphors can introduce a new path for the future development of solid-state lighting and optical contactless temperature sensing.

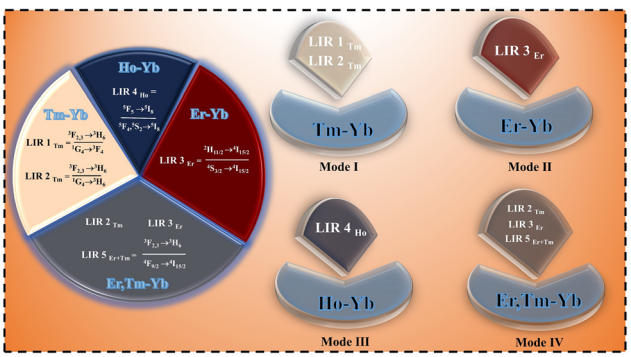

Fig. 1 Schematic representation of Modes I–IV temperature detection using LMTO:Ln^{3+} (Tm–Yb; Er–Yb; Ho–Yb; Er/Tm–Yb) phosphors.

2. Experimental section

2.1 Materials and preparation

The starting materials were La_2O_3 (AR, Aladdin), TiO_2 (AR, Aladdin), MgO (AR, Beijing Chemical Factory), Ho_2O_3 (99.99%, Aladdin), Tm_2O_3 (99.9%, Aladdin), Er_2O_3 (99.99%, Aladdin), and Yb_2O_3 (99.99%, Aladdin).

2.1.1. Synthesis of LMTO phosphors. The host LMTO was synthesized through conventional high-temperature solid-state reaction. Firstly, the raw materials, including 1 mmol La_2O_3, 1 mmol TiO_2 and 1 mmol MgO, were stoichiometrically weighted, and then ground in an agate mortar for 40 minutes. Lastly, the abovementioned reactants were transferred to the muffle furnace and heated at 1500 °C for 12 h under an ambient atmosphere.

2.1.2. Synthesis of LMTO. Ln^{3+}/Yb^{3+} phosphors: The synthesis process of such materials was basically the same as described above. Thereinto, depending on the doping concentration, x mmol of Ln_2O_3 (Ln = Er^{3+}, Tm^{3+}, Ho^{3+}, Yb^{3+}) precursor was added, while the amount of La_2O_3 added was $1 - x$ mmol.

2.1.3. Synthesis of LED. LMTO:1%Ho^{3+},5%Yb^{3+}; LMTO:4% Er^{3+},5%Yb^{3+}; LMTO:0.2%Tm^{3+},7%Yb^{3+}; and LMTO:0.2% Tm^{3+},0.05%Er^{3+},7%Yb^{3+} phosphors were mixed with silica epoxy gel A and B in a certain ratio, and then coated uniformly on a 980 nm LED chip.

2.2 Characterisation

Powder X-ray diffraction (XRD) analysis was conducted using an X-ray diffractometer equipped with Cu Kα radiation (λ = 0.15405 nm). A field-emission scanning electron microscope (FE-SEM) (Regulus-8100, Hitachi) equipped with an energy-dispersive X-ray scanning (EDS) spectrophotometer was used to observe the particle size and element composition of the phosphors. The emission spectra were recorded using an Andor SR-500i spectrometer with a 980 nm diode. Fourier transform infrared (FT-IR) and Raman spectra were determined with the help of the VERTEX80 V FT-IR spectrometer and Renishaw inVia Raman spectrometer, respectively. The temperature-dependent spectra of the powders were obtained by a constant copper thermocouple and temperature control system (TAP-02, orient-KOJI).

3. Results and discussion

3.1 Structural and composition

The phase composition of all samples in this experiment was determined by XRD technique. Firstly, as displayed in Fig. 2a, ICSD-95992 was employed as the original model, and then the Rietveld structure refinement of as-synthesized powder XRD data of the LMTO host was performed utilizing the GSAS program. The results show that the data fit well and converge to a low R-factor (R_{wp} = 4.44%, R_p = 3.93%, χ^2 = 2.66), which further demonstrates that the LMTO host is single phase (a = 5.57 Å, b = 5.58 Å, c = 7.87 Å, V = 244.755 Å^3). The expected double perovskite structure with the $P21/n$ space group of

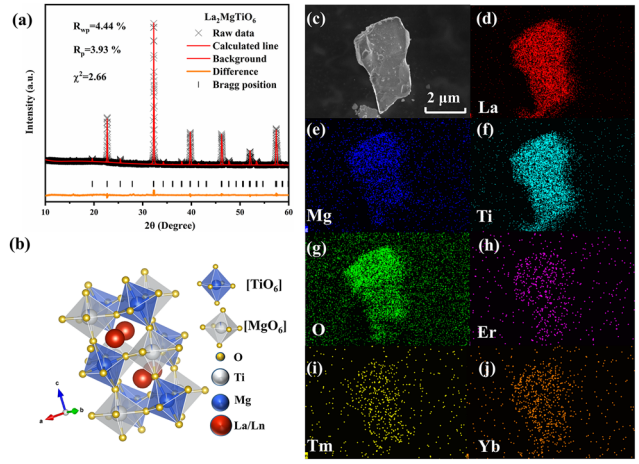

Fig. 2 (a) XRD pattern for Rietveld refinement of LMTO. (b) Crystal structure of the LMTO. (c–j) FE-SEM and elemental mapping images of the LMTO:0.2%Tm^{3+},0.05%Er^{3+},7%Yb^{3+} phosphors.

LMTO is given in Fig. 2b.[26] On this basis, the Tm–Yb; Er–Yb; Ho–Yb; and Er/Tm–Yb doped LMTO systems were prepared, and the full XRD patterns are provided in Fig. S1.† It could be found that introducing Ln^{3+} (Tm/Er/Ho/Yb) dopants does not cause the formation of impurity phases for all the samples. Considering the conservation of charge, the introduction of Ln^{3+} will replace the position of La^{3+} in the host lattice. In terms of ionic radius, it can be evaluated by the following formula:[27,28]

$$D_r = \frac{R_S - R_D}{R_S} \times 100\% \quad (1)$$

R_S and R_D represent the radii of substituted and doped ions, respectively. After substituting the values of 103.2 pm (La^{3+}) for R_S and 86.8 pm (Yb^{3+}), 88 pm (Tm^{3+}), 89 pm (Er^{3+}), and 90.1 pm (Ho^{3+}) for R_D, the resulting of D_r values are 15.9%, 14.7%, 13.8%, and 12.6%, respectively. It can be clearly seen that all D_r values are less than 30%, which is certainly further evidence that Ln^{3+} (Tm/Er/Ho/Yb) will replace La^{3+}. Therefore, the diffraction peak that slightly shifted to a higher angle in Fig. S1b† can be interpreted as lattice contraction after the substitution of La^{3+} by Tm^{3+}/Yb^{3+}. The FE-SEM image shows that the LMTO:0.2%Tm^{3+},0.05%Er^{3+},7%Yb^{3+} phosphor is an approximately 4 μm irregular particle (Fig. 2c). Meanwhile, as evidenced by the EDS spectra and corresponding element maps in Fig. S2† and Fig. 2(d–j), all elements, including Tm, Er, Yb, La, Mg, Ti and O are evenly distributed throughout the LMTO:0.2%Tm^{3+},0.05%Er^{3+},7%Yb^{3+} phosphor particles. Besides, the FE-SEM and EDS of representative LMTO:0.2% Tm^{3+},7%Yb^{3+}; LMTO:4%Er^{3+},5%Yb^{3+} and LMTO:1%Ho^{3+},5% Yb^{3+} phosphors all show satisfactory phenomena (Fig. S3–5†). In a word, the above results demonstrate that the synthesis of the target samples is successful.

3.2 Photoluminescence (PL) analysis of the LMTO:Ln^{3+} phosphors

3.2.1 Mode I: Tm–Yb system. Because there is a good matching energy between the emission of Yb^{3+} ($^2F_{5/2} \rightarrow {}^2F_{7/2}$) and the internal excitation transition of Ln^{3+} (Ho^{3+}/Er^{3+}/Tm^{3+}) upon 980 nm excitation, Yb^{3+} ions were selected as sensitizers and play an indispensable role in this experiment. As the emission spectra evidenced in Fig. S6,† the optimal Tm^{3+} content remained at 0.2%. Subsequently, Tm^{3+}/Yb^{3+}-doped samples with fixed Tm^{3+} and various Yb^{3+} contents were additionally prepared. From the UC emission spectra depicted in Fig. 3a, all of the resultant samples exhibit the characteristic emission peaks of Tm^{3+} ions (478 nm: $^1G_4 \rightarrow {}^3H_6$; 654 nm: $^1G_4 \rightarrow {}^3F_4$; 703 nm: $^3F_{2,3} \rightarrow {}^3H_6$).[29] Moreover, as shown in the illustration in Fig. 3a, the PL emission intensity would increase to the maximum value at the sensitizer Yb^{3+} ion content of 7%, and then decrease with the increment of doping content, indicating that concentration quenching would occur when x = 7%. This is because as the concentration of Yb^{3+} ions continues to increase, the sensitization effect of Yb^{3+} to Tm^{3+} is gradually replaced by back energy transfer [BET: $^2F_{7/2}$ (Yb^{3+}) + $^3H_4$ (Tm^{3+}) → $^2F_{5/2}$ (Yb^{3+}) + $^3H_6$ (Tm^{3+}) or $^2F_{7/2}$ (Yb^{3+}) + $^3F_4$ (Tm^{3+}) → $^2F_{5/2}$ (Yb^{3+}) + $^3H_6$ (Tm^{3+})].[30] Thus, the optimal doping concentration is confirmed to be LMTO:0.2%Tm^{3+},7%Yb^{3+} in the following experiments. To shed further light onto the intrinsic mechanism in the Tm^{3+}–Yb^{3+} co-doped LMTO system, the curves of UC luminescence intensity (I) *versus* excitation laser power (P) are given in Fig. 3b, which can be fitted using the following equation:[31]

$$I \propto P^n \quad (2)$$

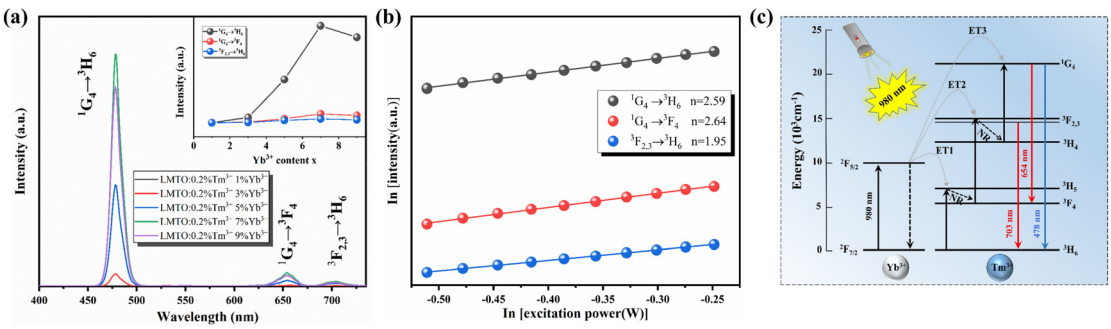

Fig. 3 Mode I (a) Emission spectra of LMTO:0.2%Tm^{3+}/xYb^{3+} phosphors. Inset: the integral curve of emission intensity with Yb^{3+} content as a variable. (b) The relationship between ln(I) and ln(P). (c) The ET processes in Tm^{3+}–Yb^{3+} co-doped LMTO system.

where n represents the exact number of photons in the involved UC mechanism. Through linear fitting, the power law exponents (n) of the emissions at 478 nm, 654 nm, and 703 nm are 2.59, 2.64, and 1.95, respectively, suggesting that $^1G_4 \rightarrow {}^3H_6$ and $^1G_4 \rightarrow {}^3F_4$ undergo a three-photon absorption process, whereas the $^3F_{2,3} \rightarrow {}^3H_6$ is a two-photon absorption process. According to the above analysis, a possible UC mechanism in the Tm^{3+}/Yb^{3+} co-doped LMTO system is proposed in Fig. 3c. Upon 980 nm excitation, the $^2F_{2/7}$ + $h\upsilon$ (980 nm) $\rightarrow$ $^2F_{2/5}$ transition of Yb^{3+} occurs, followed by energy transfer (ET) to Tm^{3+} (ET1). After non-radiative (NR) transition from $^3H_5$ to $^3F_4$ levels, the ET2 process takes place: $^3F_4$ (Tm^{3+}) + $^2F_{5/2}$ (Yb^{3+}) $\rightarrow$ $^3F_{2,3}$ (Tm^{3+}) + $^2F_{7/2}$ (Yb^{3+}). Subsequently, the population at $^3F_{2,3}$ levels decays radiatively to $^3H_6$ levels with strong red emission at 703 nm. Next, the electrons at $^3F_{2,3}$ level are re-populated at $^3H_4$ level through NR processes. As mentioned above, the three-photon emission of $^1G_4 \rightarrow {}^3H_6$ and $^1G_4 \rightarrow {}^3F_4$ could be achieved through ET3: $^3H_4$ (Tm^{3+}) + $^2F_{5/2}$(Yb^{3+}) $\rightarrow$ $^1G_4$ (Tm^{3+}) + $^2F_{7/2}$ (Yb^{3+}).

3.2.2 Mode II: Er–Yb system. Similar to that in the Tm–Yb system, Er–Yb co-doped LMTO phosphors also show amazing potential. First, the concentrations of Er^{3+} and Yb^{3+} were fixed successively. The UC emission spectra of Er–Yb co-doped LMTO phosphors are displayed in Fig. S7† and Fig. 4a. Each sample has the same emission band characteristics, corresponding to the $^2H_{11/2} \rightarrow {}^4I_{15/2}$ (534 nm), $^4S_{3/2} \rightarrow {}^4I_{15/2}$ (554 nm) and $^4F_{9/2} \rightarrow {}^4I_{15/2}$ (662 nm) transitions of Er^{3+} ions, respectively.[32] Although the UC luminescence intensity of Er^{3+} is proportional to the proportion of Yb^{3+} ion doping in Fig. 4a, the impurity $La_2Ti_2O_7$ appears when the doping amount of Yb^{3+} ions reaches 6% (Fig. S8†). For experimental accuracy, the optimal doping content of the Er–Yb co-doped LMTO system in this experiment was determined at 4%Er^{3+} and 5%Yb^{3+}. From the ln(I)–ln(P) plot of the LMTO:4%Er^{3+},5%Yb^{3+} phosphor in Fig. 4b, the obtained n values are 2.17, 2.33 and 2.03 for the UC peaks at ~534, 554 and 662 nm, respectively. These results indicate that two-photon absorption dominates the UC process of the Er–Yb system. Therefore, the possible energy transition mechanism between Er^{3+}–Yb^{3+} ions is depicted in Fig. 4c. Upon 980 nm excitation, the electrons at $^4I_{15/2}$ of Er^{3+} jumped to the $^4I_{11/2}$ and $^4F_{7/2}$ levels, successively, *via* two consecutive ET processes through Yb^{3+} ions (ET1 and ET3). Then, after the NR transition from $^4F_{7/2}$ to $^2H_{11/2}$ and $^4S_{3/2}$ levels, strong green emissions at 534 and 554 nm are realized. In general, the red emission at 662 nm originates from the NR transition of electrons on the $^4I_{11/2}$ to the $^4I_{13/2}$ level, which absorbs the ET of Yb^{3+} ions and transitions to the $^4F_{9/2}$ level (ET2).

3.2.3 Mode III: Ho–Yb system. Fig. S9† and Fig. 5a display the UC spectra of Ho^{3+}–Yb^{3+} co-doped LMTO phosphors upon 980 nm excitation. The primary band in the green emission region with maxima at 543 nm and the faint red emission at 652 nm are ascribed to the $^5F_4$,$^5S_2 \rightarrow {}^5I_8$ and the $^5F_5 \rightarrow {}^5I_8$ transition of Ho^{3+} ions, respectively.[33] It is not difficult to find that the optimal doping ratio in the Ho–Yb system is 1%Ho^{3+}, 5% Yb^{3+}. Similarly, the n values were obtained as 2.25 (green) and 2.31 (red), which indicates that the emissions in the LMTO host both involved the two-photon process (Fig. 5b). As shown in the ET mechanism diagram constructed in Fig. 5c, Yb^{3+} ions can also be used as an excellent sensitizer for ET process in Ho^{3+}–Yb^{3+} co-doped LMTO phosphors. Similar to the above discussion, the Yb^{3+} ion first absorbs a phonon from $^2F_{7/2}$ to $^2F_{5/2}$ for the first energy transfer after completing the transition (ET1). Then, two different emissions are obtained: (1) green emission: $^2F_{5/2}$ (Yb^{3+}) + $^5I_6$ (Ho^{3+}) $\rightarrow$ $^2F_{7/2}$ (Yb^{3+}) + $^5F_4$,$^5S_2$ (Ho^{3+}) (ET3); (2) red emission: $^5I_6$ (Ho^{3+}) $\rightarrow$ $^5I_7$ (Ho^{3+}) (NR) and $^2F_{5/2}$ (Yb^{3+}) + $^5I_7$ (Ho^{3+}) $\rightarrow$ $^2F_{7/2}$ (Yb^{3+}) + $^5F_5$ (Ho^{3+}). It is inferred from the above discussion that the red emission intensity in the Ho–Yb system largely depends on the NR transition process, which is closely related to the host phonon energy:[34]

$$W(T) = W(0)\left[\frac{\exp\left(\frac{h\upsilon}{kT}\right)}{\exp\left(\frac{h\upsilon}{kT}\right)-1}\right]^{\Delta E/h\upsilon} \quad (3)$$

where $h\upsilon$ is the phonon energy, $W(0)$ and $W(T)$ are the NR transition rate at temperature 0 and T K, and ΔE is the energy gap. As displayed in Fig. S10 and S11,† the Raman and FT-IR spectra of the blank LMTO were tested to determine the phonon energy of the host. It can be clearly seen that the strongest wavenumbers in the Raman and FT-IR spectra are 447 cm^{-1} and 578 cm^{-1}, respectively. The former is associated with T_{2g}

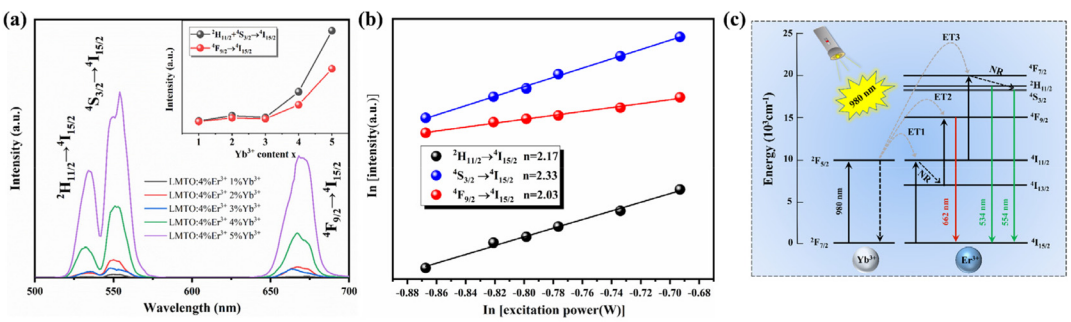

Fig. 4 Mode II (a) Emission spectra of LMTO:4%Er^{3+}/xYb^{3+} phosphors. Inset: the integral curve of emission intensity with Yb^{3+} content as a variable. (b) The relationship between ln(I) and ln(P). (c) The ET processes in Er^{3+}–Yb^{3+} co-doped LMTO system.

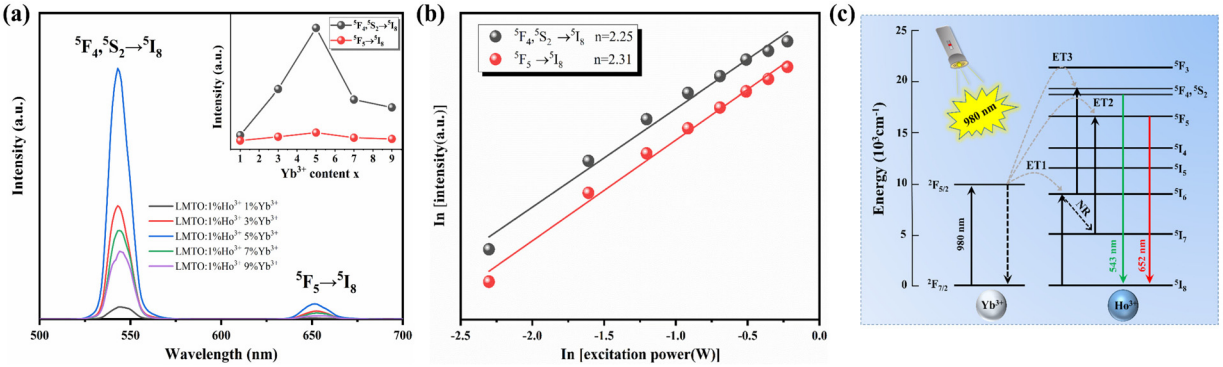

Fig. 5 Mode III (a) Emission spectra of LMTO:1%Ho^{3+}/xYb^{3+} phosphors. Inset: the integral curve of emission intensity with Yb^{3+} content as a variable. (b) The relationship between ln(*I*) and ln(*P*). (c) The ET processes in Ho^{3+}–Yb^{3+} co-doped LMTO system.

vibration mode caused by tilted $[MgO_6]^{4-}$ and $[TiO_6]^{2-}$ octahedron, and the latter is assigned to Ti–O stretching vibration, which means that the phonon energy of LMTO is in the range of 400–600 cm^{-1}, while the ΔE of $^5I_6$ and $^5I_7$ is about 3450 cm^{-1}.[35,36] Based on the energy gap law, NR processes will hardly occur if the ΔE in activators is five times higher than that of the vibrational frequency of the host, which explains the extremely weak red emission in the Ho–Yb system.[32]

3.2.4 Mode IV: Tm, Er–Yb system. The above phenomena show that the Tm–Yb, Er–Yb and Ho–Yb systems exhibit excellent UC luminescence properties, including strong blue, green, red emission. Therefore, in the next experiment, we designed a series of Ln^{3+} (Ho^{3+}, Er^{3+}, Tm^{3+})-Yb^{3+} co-doped double perovskite LMTO phosphors, hoping to achieve other luminescence colours, preferably, white emission in Ln–Yb co-doped double perovskite LMTO phosphors by adjusting the ratio of red, green and blue. However, as shown in the UC emission spectra illustrated in Fig. 6a, both LMTO:0.2%Tm^{3+},0.05%Er^{3+},0.05% Ho^{3+},7%Yb^{3+} and LMTO:0.2%Tm^{3+},0.05%Ho^{3+},7%Yb^{3+} phosphors exhibit UC phenomena dominated by the intrinsic emissions of Ho^{3+} ($^5F_4$,$^5S_2 \rightarrow ^5I_8$ and $^5F_5 \rightarrow ^5I_8$) ions upon 980 nm excitation. Fortunately, the UC emission spectrum of the LMTO:0.2%Tm^{3+},0.05%Er^{3+},7%Yb^{3+} phosphor consists of three regions clearly visible in blue (Tm^{3+}: $^1G_4 \rightarrow ^3H_6$), green (Er^{3+}: $^2H_{11/2}$/$^4S_{3/2} \rightarrow ^4I_{15/2}$), and red ($Er^{3+}$: $^4F_{9/2} \rightarrow ^4I_{15/2}$; Tm^{3+}: $^3F_{2,3} \rightarrow ^3H_6$), which meets the necessary conditions for white emission. Moreover, as shown in Fig. S12,† the LMTO:0.2%Tm^{3+},0.05% Er^{3+},7%Yb^{3+} phosphor is expected to achieve white emission by adjusting the doping concentration of the activator. For the Er, Tm–Yb system, the electron transition process is basically consistent with Er–Yb and Tm–Yb co-doped LMTO phosphors (Fig. 6b). The only difference is that the ΔE between the red emission of Er^{3+} ions at 662 nm and that of Tm^{3+} ions at 654 nm is so close that the presence of the cross-relaxation (CR) process leads to a decrease in blue emission (Tm^{3+}: $^1G_4 \rightarrow ^3H_6$) and a predominance of Er^{3+} ions in the red region (Er^{3+}: $^4F_{9/2} \rightarrow ^4I_{15/2}$) [CR: $^4I_{15/2}$ (Er^{3+}) + $^1G_4$ (Tm^{3+}) → $^4F_{9/2}$ (Er^{3+}) + $^3F_4$ (Tm^{3+})].

3.3 Multicolour display performance

For the sake of proving whether the representative phosphors selected from the above Tm–Yb, Ho–Yb, Er–Yb and Tm, Er–Yb systems can be applied to solid-state lighting, LED devices were fabricated by coating LMTO:1%Ho^{3+},5%Yb^{3+}; LMTO:4% Er^{3+},5%Yb^{3+}; LMTO:0.2%Tm^{3+},7%Yb^{3+}; and LMTO:0.2% Tm^{3+},0.05%Er^{3+},7%Yb^{3+} phosphors on the surface of a 980 nm chip, as displayed in Fig. 7. Obviously, both the untreated phosphors excited by 980 nm (30 W cm^{-2}) and LED devices after passing 200 mA current emit satisfactory pure-colour

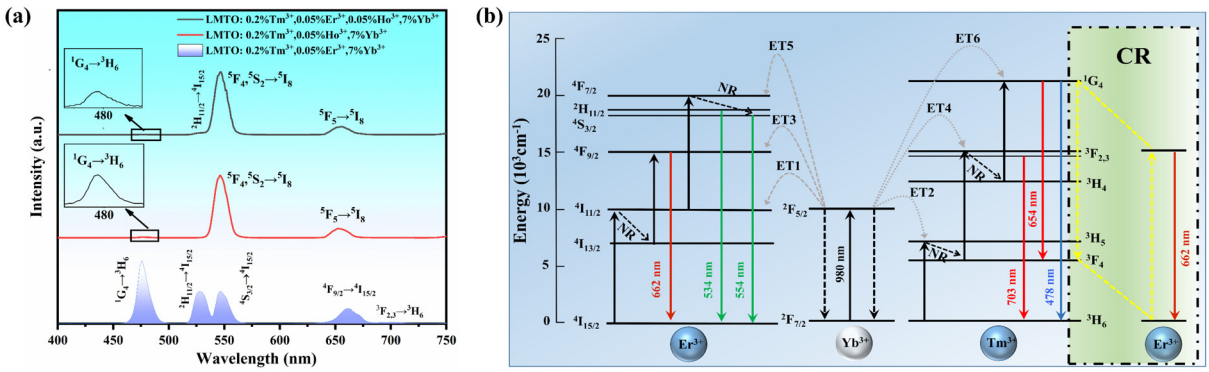

Fig. 6 Mode IV (a) Emission spectra of LMTO:0.2%Tm^{3+},0.05%Er^{3+},0.05%Ho^{3+},7%Yb^{3+}; LMTO:0.2%Tm^{3+},0.05%Ho^{3+},7%Yb^{3+} and LMTO:0.2% Tm^{3+},0.05%Er^{3+},7%Yb^{3+} phosphors. (b) The ET processes in Er^{3+}, Tm^{3+}–Yb^{3+} co-doped LMTO system.

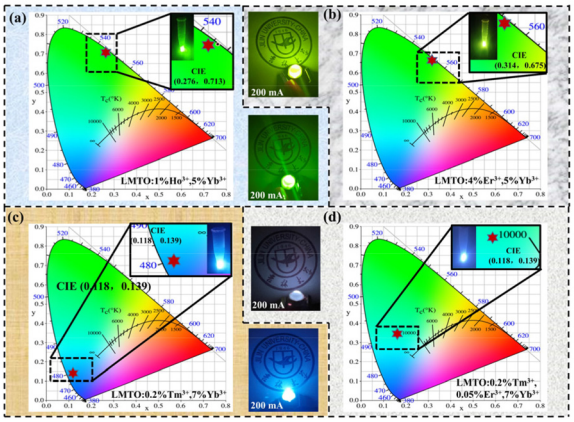

Fig. 7 CIE chromatic coordinates of (a) LMTO:1%Ho^{3+},5%Yb^{3+}; (b) LMTO:4%Er^{3+},5%Yb^{3+}; (c) LMTO:0.2%Tm^{3+},7%Yb^{3+} and (d) LMTO:0.2%Tm^{3+},0.05%Er^{3+},7%Yb^{3+} phosphors. Inset: digital graphics of the obtained powder upon 980 nm excitation (30 W cm^{-2}) and packaged LED devices under 200 mA current.

emission. Meanwhile, colour purity is one of the key parameters describing the calorific properties of the prepared phosphors, which could be calculated as follows:[37,38]

$$\text{Color purity} = \frac{\sqrt{(x-x_i)^2+(y-y_i)^2}}{\sqrt{(x_d-x_i)^2+(y_d-y_i)^2}} \times 100\% \quad (4)$$

Here, the (x, y), (x_d, y_d), and (x_i, y_i) are associated with the CIE coordinates of LMTO:1%Ho^{3+},5%Yb^{3+}; LMTO:4%Er^{3+},5%Yb^{3+}; and LMTO:0.2%Tm^{3+},7%Yb^{3+} phosphors' visible region emission, dominant emission and white illumination (0.3101, 0.3162). Hence, based on eqn (4), in addition to near-white-light emission of the LMTO:0.2%Tm^{3+},0.05%Er^{3+},7%Yb^{3+} phosphor, the color purity of LMTO:1%Ho^{3+},5%Yb^{3+}; LMTO:4%Er^{3+},5%Yb^{3+}; and LMTO:0.2%Tm^{3+},7%Yb^{3+} phosphors can be calculated, which reaches up to 91.8%, 93.4% and 92.2%, respectively (Table S1†). It is further verified that the Ho^{3+}/Er^{3+}/Tm^{3+}-activated LMTO phosphors with higher color purity compared with the previously proposed may have promising applications in white LEDs as a green-emitting or blue-emitting phosphor.[39,40]

3.4.1 Temperature-sensing properties of Modes I–IV. LIR technology is based on the repopulation of electrons in TCLs or non-TCLs in Ln^{3+} ions or transition metal ions.[41–43] As we all know, it is more difficult for TCLs to distinguish between the two emission bands due to the relatively small ΔE (200–2000 cm^{-1}).[44] Meanwhile, according to the sensitivity formula ($S_r = \Delta E/kT^2$), the small ΔE of TCLs greatly restricts the emergence of high-sensitivity thermometers.[45] While the LIR technique based on non-TCLs is no longer limited by ΔE, the two monitored energy levels can hardly reach thermal equilibrium because they do not satisfy the Boltzmann distribution, and the final sensitivity is affected by the energy conversion from the higher energy level to the lower energy level. It can be seen that there are certain shortcomings in adopting a single principle of LIR optical temperature measurement. Inspired by these, we systematically explored the separate LIR technology based on TCL (Mode II) or non-TCLs (Mode I and III), and realized the combination of the former in Mode IV, greatly improving the accuracy of temperature sensing.

3.4.2 Mode I: Tm–Yb system. In the Tm–Yb system, the luminescence intensity ratios of Tm^{3+} ions, LIR 1_{Tm} = $^3F_{2,3} \rightarrow {}^3H_6/{}^1G_4 \rightarrow {}^3F_4$ and LIR 2_{Tm} = $^3F_{2,3} \rightarrow {}^3H_6/{}^1G_4 \rightarrow {}^3H_6$, were used as the original parameters for optical temperature measurement (Mode I). The thermal evolution emission spectra of the LMTO:0.2%Tm^{3+},7%Yb^{3+} phosphor recorded from 313 K to 573 K are described in Fig. 8a. From the illustration, one can clearly see that the intensities of the $^1G_4 \rightarrow {}^3F_4$ and $^1G_4 \rightarrow {}^3H_6$ emissions are quenched dramatically as the temperature rises, whereas the intensity of the $^3F_{2,3} \rightarrow {}^3H_6$ emission is basically unaffected by temperature change. Therefore, based on such obvious temperature dependence, two kinds of LIR models $^3F_{2,3} \rightarrow {}^3H_6/{}^1G_4 \rightarrow {}^3F_4$ (LIR 1_{Tm}) and $^3F_{2,3} \rightarrow {}^3H_6/{}^1G_4 \rightarrow {}^3H_6$ (LIR 2_{Tm}) were constructed as the temperature-detecting signal. For the non-TCLs, it is difficult to fill them by thermal activation due to their large energy gaps. Under this situation, all calculated LIRs in the Tm–Yb system can be approximated with the following formula:[46]

$$\text{LIR} = A\exp\left(-\frac{B}{T}\right) + C \quad (5)$$

where T is the absolute temperature; A, B, and C are fitting constants. Firstly, the results in Fig. 8b clearly show that LIR 1_{Tm} is highly fitted to eqn (5). According to previous reports, in order to facilitate the evaluation of the heat sensing performance of the synthesized materials, two important parameters, absolute sensitivity (S_a) and relative sensitivity (S_r), are usually introduced to accurately compare the thermal sensitivity properties between different thermometers, which can be calculated as shown below:[47,48]

$$S_a = \frac{d\text{LIR}}{dT} = A\exp\left(-\frac{B}{T}\right) \times \left(\frac{B}{T^2}\right) \quad (6)$$

$$S_r = \frac{1}{\text{LIR}}\frac{d\text{LIR}}{dT} = \frac{A\exp\left(-\frac{B}{T}\right)}{A\exp\left(-\frac{B}{T}\right)+C} \times \frac{B}{T^2} \times 100\%. \quad (7)$$

The S_a and S_r values were then calculated by eqn (6) and (7), as presented in Fig. 8c. What is surprising is that the values of $S_{a\ Max}$ and $S_{r\ Max}$ of the LIR 1_{Tm} mode reach as high as 4.94% K^{-1} and 1.92% K^{-1}, respectively. On the other hand, the measured diagram of the variation of LIR 2_{Tm} with temperature can also be well fitted by eqn (5) in Fig. 8d. Combining eqn (6) and (7), the LIR 2_{Tm} model also has excellent temperature sensitivity ($S_{r\ Max}$ = 1.63% K^{-1}, $S_{a\ Max}$ = 3.32% K^{-1}, Fig. 8e). In Mode I based on Tm–Yb system, when an error occurs in one of the LIR models, the other LIR model can be corrected immediately. Hence, this self-calibrating thermo-

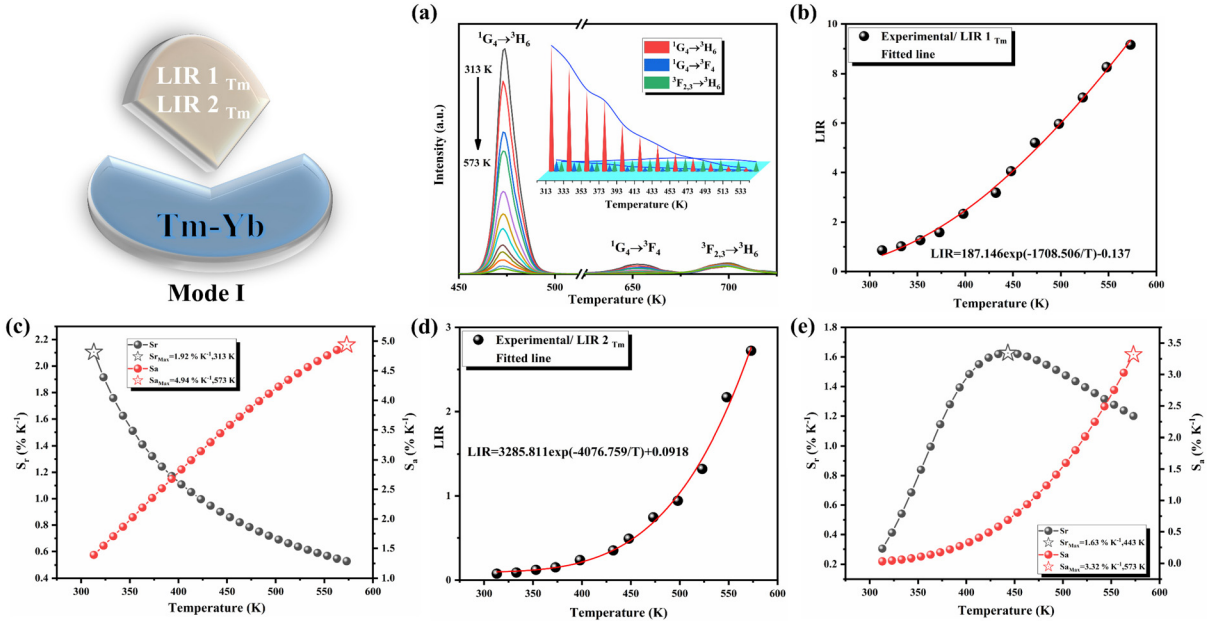

Fig. 8 Mode I (a) Temperature-dependent PL spectra of LMTO:0.2%Tm^{3+},7%Yb^{3+} phosphor. Inset: the PL emission intensity *versus* various temperatures. (b and c) LIR 1_{Tm} = $^3F_{2,3} \rightarrow {}^3H_6/{}^1G_4 \rightarrow {}^3F_4$ and its S_a/S_r values at various temperatures. (d and e) LIR 2_{Tm} = $^3F_{2,3} \rightarrow {}^3H_6/{}^1G_4 \rightarrow {}^3H_6$ and its S_a/S_r values at various temperatures.

meter significantly enhances the accuracy of temperature monitoring.

3.4.3 Mode II: Er–Yb system. In the Er–Yb system, the LIR of Er^{3+} ions, LIR 3_{Er} = $^2H_{11/2} \rightarrow {}^4I_{15/2}/{}^4S_{3/2} \rightarrow {}^4I_{15/2}$, was used as the original parameter for optical temperature measurement (Mode II). The UC emission spectra of the LMTO:4%Er^{3+},5% Yb^{3+} phosphor at various temperatures is presented in Fig. 9a (λ_{ex} = 980 nm, 313–573 K). Moreover, compared with the integral emission intensity of TCLs ($^2H_{11/2}$ and $^4S_{3/2}$), it is obvious that the $^4S_{3/2} \rightarrow {}^4I_{15/2}$ emission intensity is always suppressed as the temperature increases and, finally, becomes lower than that of $^2H_{11/2} \rightarrow {}^4I_{15/2}$ emission intensity (Fig. 9b). This is because the energy difference between the TCLs is much smaller than that in the non-TCLs, so electrons at the $^4S_{3/2}$ level can reach the $^2H_{11/2}$ level by absorbing the lattice vibrational energy generated with increasing temperature. For TCLs, the LIR 3_{Er} in the Er–Yb system can be calculated using the following formula:[49]

$$\mathrm{LIR} = \frac{I_2}{I_1} = \frac{N_2 h\upsilon_2 A_2}{N_1 h\upsilon_1 A_1} = \frac{g_2 \upsilon_2 A_2}{g_1 \upsilon_1 A_1} \exp\left(\frac{-\Delta E}{kT}\right) = B \exp\left(\frac{-\Delta E}{kT}\right) \quad (8)$$

where N_i, h, υ_i and A_i denote the electron population, Planck's constant, the frequency and the spontaneous emission rate of the corresponding transitions, respectively. B and k are the fitted parameter and Boltzmann constant; ΔE is the energy gap between the TCLs of Er^{3+}. The curve of LIR 3_{Er} changes with temperature after fitting the experimental data with eqn (8), as shown in Fig. 9c. It is found that the values of B and $\Delta E/k$ are 13.9 and 1101.922, respectively. According to the results, the energy gap of the TCLs is about 760 cm^{-1}. As previously discussed, the TCLs of Er^{3+} ion have a significant temperature-dependent population redistribution ability (PRA), which can be accurately evaluated by the following formulas:[50]

$$\mathrm{PRA} = \frac{I_U}{I_U + I_L} = \frac{I_H}{I_H + I_S} \quad (9)$$

$$\mathrm{PRA} = \frac{B}{B + \exp\left(\frac{\Delta E}{kT}\right)} \quad (10)$$

where I_U and I_L are upper ($^2H_{11/2}$) and lower ($^4S_{3/2}$) level emission intensity, respectively. Combining eqn (8) and (9), the final PRA can be redefined in eqn (10). With the increasing temperature, the PRA value of LMTO:4%Er^{3+},5%Yb^{3+} phosphor soared from 0.29 (313 K) to 0.67 (573 K), further confirming that the population between TCLs is mainly affected by ambient temperature (Fig. 9d). Therefore, LMTO:4%Er^{3+},5% Yb^{3+} phosphor has the potential to become a high-sensitivity optical thermometer. For TCLs, the S_a and S_r in Er–Yb system can be written as:[51]

$$S_a = \left|\frac{\partial \mathrm{LIR}}{\partial T}\right| = \mathrm{LIR}\left(\frac{\Delta E}{kT^2}\right) = B\left(\frac{\Delta E}{kT^2}\right) \exp\left(\frac{-\Delta E}{kT^2}\right) \quad (11)$$

$$S_r = \left|\frac{1}{\mathrm{LIR}} \frac{d\mathrm{LIR}}{dT}\right| = \frac{\Delta E}{kT^2}. \quad (12)$$

The S_a and S_r values of LMTO:4%Er^{3+},5%Yb^{3+} phosphor, calculated by eqn (11) and (12), are depicted in Fig. 9e. Obviously, the LMTO:4%Er^{3+},5%Yb^{3+} phosphor exhibits outstanding S_r and S_a upon 980 nm excitation; the $S_{r\ Max}$ is 1.13% K^{-1} (313 K) and the $S_{a\ Max}$ is 0.68% K^{-1} (563 K) of LIR 3_{Er} in the Er–Yb system.

3.4.4 Mode III: Ho–Yb system. In the Ho–Yb system, the luminescence intensity ratios of Ho^{3+} ions, LIR 4 $_{Ho}$ = $^5F_5 \rightarrow$

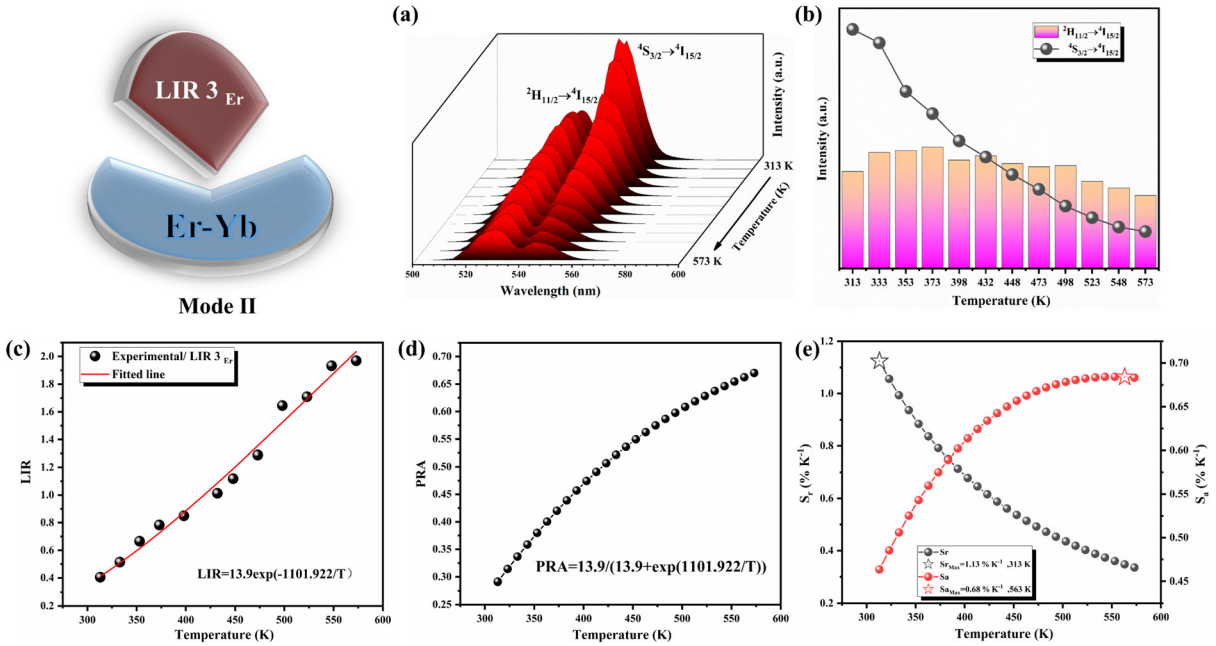

Fig. 9 Mode II (a) Temperature-dependent PL spectra of the LMTO:4%Er^{3+},5%Yb^{3+} phosphor. (b) Integrated emission intensities of TCL emission. (c) LIR 3_{Er}; (d) PRA; and (e) S_a/S_r values at various temperatures.

$^5I_8/^5F_4,^5S_2 \rightarrow {}^5I_8$, were used as the original parameters for optical temperature measurement (Mode III). Fig. 10a displays the emission spectra of LMTO:1%Ho^{3+},5%Yb^{3+} phosphor at various temperatures. In order to more intuitively reflect the different response capabilities of $^5F_4,^5S_2 \rightarrow {}^5I_8$ and $^5F_5 \rightarrow {}^5I_8$ emission to external temperature, Fig. 10b displays the normalized luminescence intensity of LMTO:1%Ho^{3+},5%Yb^{3+} phosphor at 543 nm and 652 nm. It is easier to infer that the effect of temperature on the emission intensity of $^5F_4,^5S_2 \rightarrow {}^5I_8$ transition is obviously greater than that of $^5F_5 \rightarrow {}^5I_8$ transition, which can be explained by the Mott–Seitz model:[52]

$$K_{nr} \propto \exp\left(-\frac{\Delta E}{kT}\right) \quad (13)$$

where K_{nr} is the NR probability, and ΔE, k and T are the same as in eqn (3). From this, it can be concluded that temperature is also an important parameter affecting the NR process. The lattice vibration in the LMTO host is intensified with the increase of temperature, which makes up for the number of phonons in the host to some extent and promotes the emergence of the NR process [$^5I_6$ (Ho^{3+}) $\rightarrow {}^5I_7$ (Ho^{3+})]. Therefore, the red-green ratio of the phosphors at high temperature is obviously enhanced compared to that at room temperature (Fig. S13†). According to eqn (5), Fig. 10c shows the relationship between LIR 4_{Ho} and absolute temperature. The results show that the experimental data can be fitted by a nonlinear relationship, LIR = 9.156exp(−1920.351/T) + 0.082. After that, the $S_{r\ Max}$ (0.58% K^{-1}, 423 K) and $S_{a\ Max}$ (0.18% K^{-1}, 573 K) values are calculated in Fig. 10d by eqn (6) and (7), which is smaller than those of Mode I and Mode II. Fortunately, compared with other Ho^{3+}-activated thermometers, the results are satisfactory.[53,54]

3.4.5 Mode IV: Tm, Er–Yb system. In the Tm, Er–Yb system, the luminescence intensity ratios of Er^{3+} and Tm^{3+} ions, LIR $2_{Tm} = {}^3F_{2,3} \rightarrow {}^3H_6/{}^1G_4 \rightarrow {}^3H_6$, LIR $3_{Er} = {}^2H_{11/2} \rightarrow {}^4I_{15/2}/{}^4S_{3/2} \rightarrow {}^4I_{15/2}$ and LIR $5_{Er+Tm} = {}^3F_{2,3} \rightarrow {}^3H_6/{}^4F_{9/2} \rightarrow {}^4I_{15/2}$ were used as the original parameters for optical temperature measurement (Mode IV). The three-dimensional temperature-dependent emission spectra of the LMTO:0.2%Tm^{3+},0.05% Er^{3+},7%Yb^{3+} phosphor recorded from 313 K to 573 K are described in Fig. 11a. Because the characteristic emission peak intensity of the phosphor shows an obvious temperature-dependent phenomenon (Tm^{3+}: $^1G_4 \rightarrow {}^3H_6$, $^3F_{2,3} \rightarrow {}^3H_6$; Er^{3+}: $^2H_{11/2}/{}^4S_{3/2} \rightarrow {}^4I_{15/2}$, $^4F_{9/2} \rightarrow {}^4I_{15/2}$), as displayed in Fig. S14,† the temperature measurement performance of the phosphor is worthy of systematic study. Among them, LIR 2_{Tm} and LIR 5_{Er+Tm} (non-TCLs) were fitted by eqn (5), and LIR 3_{Er} (TCLs) was fitted by eqn (8), as shown in Fig. 11b. Similarly, the S_a and S_r values of LIR 2_{Tm} and LIR 5_{Er+Tm} were calculated by eqn (6) and (7), while the S_a and S_r values of LIR 3_{Er} were calculated by eqn (11) and (12). The calculated S_a are plotted in Fig. 11c. The maximum values of S_a are found to be 0.81% K^{-1}, 1.47% K^{-1} and 1.06% K^{-1} of LIR 2_{Tm}, LIR 3_{Er} and LIR 5_{Er+Tm}, respectively. More interestingly, as shown in Fig. 11d, the optimal S_r values of the three temperature measurement schemes in the Tm, Er–Yb system are located in three highly identifiable temperature ranges: low temperature (T < 323 K, LIR 3_{Er}, $S_{r\ Max}$ = 1.09% K^{-1}), medium temperature (323 K < T < 393 K, LIR 5_{Er+Tm}, $S_{r\ Max}$ = 1.21% K^{-1}) and high temperature (T > 393 K, LIR 2_{Tm}, $S_{r\ Max}$ = 1.36% K^{-1}). Therefore, in the optical thermometer Mode IV based on the Er, Tm–Yb system,

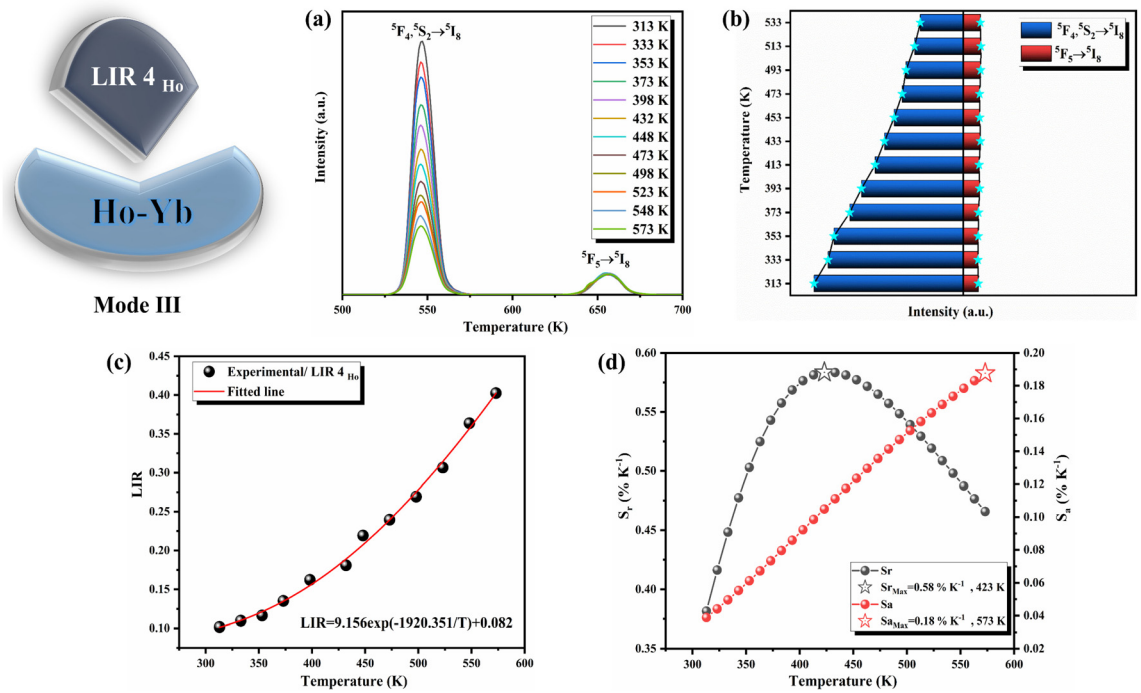

Fig. 10 Mode III (a) Temperature-dependent PL spectra of LMTO:1%Ho^{3+},5%Yb^{3+} phosphor. (b) The PL emission intensity *versus* various temperatures. The (c) LIR 4_{Ho} and (d) S_a/S_r values as a function of temperature of LMTO:1%Ho^{3+},5%Yb^{3+} phosphor.

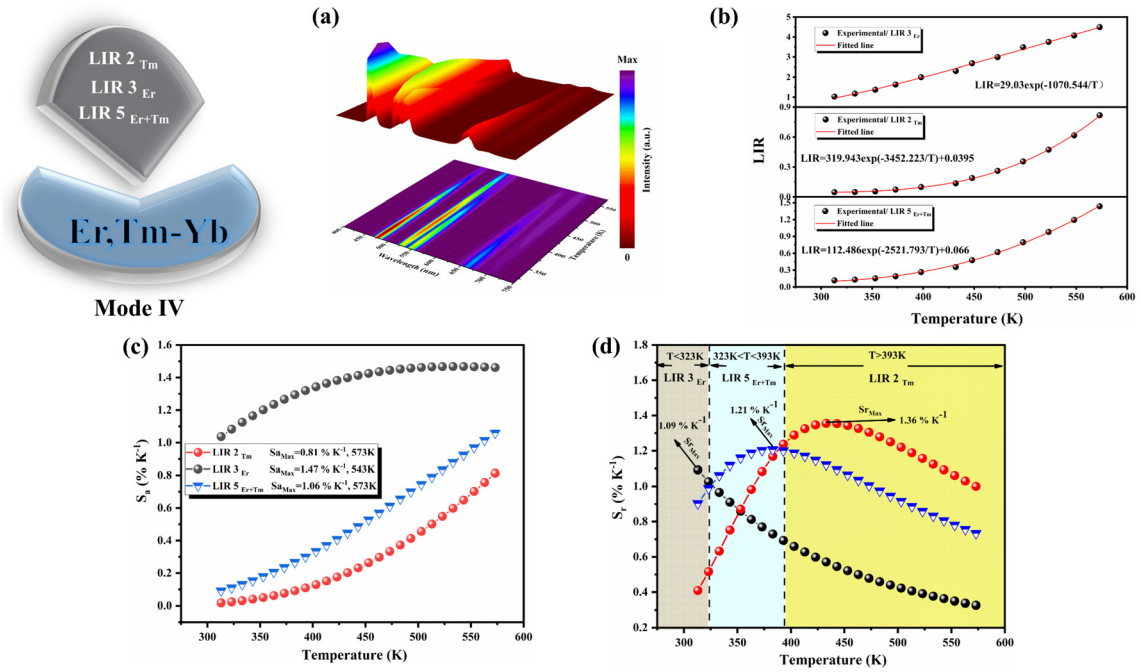

Fig. 11 Mode IV (a) Three-dimensional temperature-dependent PL spectra of LMTO:0.2%Tm^{3+},0.05%Er^{3+},7%Yb^{3+} phosphor. The (b) LIR; (c) S_a (d) S_r values as a function of temperature.

the LIR scheme with high sensitivity can be selected in a specific temperature range. This upgraded version of high-precision self-calibrating optical thermometer has rarely appeared in previous reports. It overcomes the disadvantage of small range in traditional temperature measurement and greatly improves the possibility of commercial application.

3.4.6 Performance exploration of temperature measurement Modes I–IV. In summary, all four luminescence thermo-

meter modes based on LMTO:Ln^{3+} (Ho^{3+}, Er^{3+}, Tm^{3+}) phosphors exhibit excellent sensitivity. After comparing temperature measurement performance to previously reported Ln^{3+}-based (*e.g.*, Ho^{3+}, Er^{3+}, Tm^{3+}) optical thermometers, their superiority is better demonstrated (Table S2†). Besides, a qualified optical thermometer not only needs high sensitivity, but also excellent stability and repeatability. In this experiment, as shown in Fig. 12(a and b), we continuously measured the temperature measurement Mode I–IV 50 times in the ambient temperature of 333 K and calculated the temperature uncertainty (δT) using the following formula:[55]

$$\delta T = \frac{1}{S_r}\frac{\delta \mathrm{LIR}}{\mathrm{LIR}} \quad (14)$$

where δLIR and LIR are the standard deviation and average value of 50 measurements, respectively. The curve of the variation of δT values with temperature changes obtained from eqn (14) are shown in Fig. S15 and Table S3.† In addition, five cyclic tests were carried out on Modes I–IV, and the results are displayed in Fig. 12(c and d) (333–525 K). Repeatability (R) can be defined as:[56]

$$R = 1 - \frac{\max(|\mathrm{LIR_C} - LIR_i|)}{\mathrm{LIR_C}} \quad (15)$$

where $\mathrm{LIR_i}$ and $\mathrm{LIR_C}$ are the measured value and average value. As can be seen from the Fig. 12(c and d), the repetition rate of each mode is more than 90%, and the Mode III system based on Er–Yb is as high as 98.5% (Table S3†). Therefore, low δT values and high R values indicate that the four temperature measurement modes constructed are sufficient to occupy a place in the commercial non-contact optical thermometer field because of their excellent sensitivity, stability and repeatability.

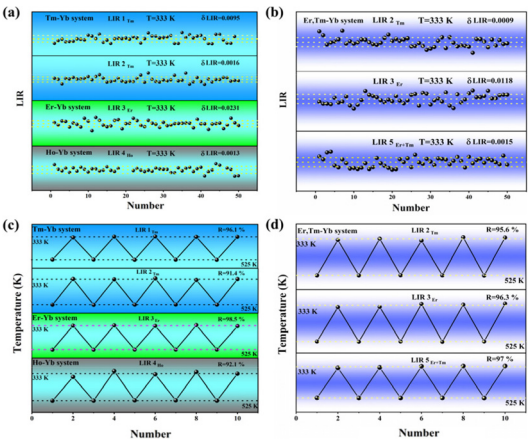

Fig. 12 (a and b) LIR distribution at 333 K for 50 consecutive measurements. (c and d) Repeatability heating–cooling cycles between 333 and 523 K of Modes I–IV.

4. Conclusions

In summary, based on the excellent lanthanide compatibility and low phonon energy of double perovskite LMTO, four different systems of high-performance multifunctional phosphors were successfully prepared (Tm–Yb; Er–Yb; Ho–Yb; Er/Tm–Yb). After systematic analysis results of the UC emission spectra, the optimal doping concentration of each system was selected. On this basis, four kinds of LED devices with intense emission were fabricated (blue: Tm–Yb; green: Er–Yb and Ho–Yb; near-white: Er/Tm–Yb). It is noteworthy that both green and blue emission have high colour purity greater than 90%, and there is a high possibility of white emission depending on adjusting the doping concentration in the Er/Tm–Yb system. On the other hand, the optical thermometers (Modes I–IV) constructed in this experiment also exhibit superior temperature sensing performance. The temperature measurement Modes I–III have a single-emitting center based on TCLs (Mode II: Er) and non-TCLs (Mode I: Tm and Mode III: Ho). Among them, the performance of Mode I is most prominent (LIR 1_{Tm}: $S_{r\ Max}$ = 1.92% K^{-1}, $S_{a\ Max}$ = 4.94% K^{-1}; LIR 2_{Tm}: $S_{r\ Max}$ = 1.63% K^{-1}, $S_{a\ Max}$ = 3.32% K^{-1}). As for Mode IV, an accurate partition self-calibrating thermometer with dual-emission centers was designed, which can measure temperature with high sensitivity in an ultra-wide temperature range (333–573 K, $S_{r\ Max}$ > 1% K^{-1}). Finally, this experiment verifies the excellent stability and repeatability of the four modes. On account of these results, all as-prepared excellent lanthanide compatible multifunctional phosphors provide a new direction for development in the field of luminescence and temperature measurement.

Author contributions

Keming Zhu and Hanyu Xu designed, executed, and analyzed experiments. Keming Zhu wrote and revised manuscripts. Zhiying Wang assisted in performance testing. Zuoling Fu provided revision guidance, suggestions and financial support.

Conflicts of interest

There are no conflicts to declare.

Acknowledgements

This research was supported by the National Science Foundation of China (Grant No. 11874182) and Key Projects of Jilin Province Science and Technology Development Plan (20230201060GX). The authors thank the Instrument and Equipment Sharing Platform, college of physics (Jilin University).

References

1 N. Hamon, A. Roux, M. Beyler, J. C. Mulatier, C. Andraud, C. Nguyen, M. Maynadier, N. Bettache, A. Duperray, A. Grichine, S. Brasselet, M. Gary-Bobo, O. Maury and R. Tripier, Pyclen-Based Ln(III) Complexes as Highly Luminescent Bioprobes for In Vitro and In Vivo One- and Two-Photon Bioimaging Applications, *J. Am. Chem. Soc.*, 2020, **142**, 10184–10197.

2 J. P. Xue, Z. K. Yu, H. M. Noh, B. R. Lee, B. C. Choi, S. H. Park, J. H. Jeong, P. Du and M. J. Song, Designing multi-mode optical thermometers via the thermochromic $LaNbO_4$:Bi^{3+}/Ln^{3+} (Ln=Eu, Tb, Dy, Sm) phosphors, *Chem. Eng. J.*, 2021, **415**, 128977.

3 C. Li, Z. Hou, C. Zhang, P. Yang, G. Li, Z. Xu, Y. Fan and J. Lin, Controlled Synthesis of Ln^{3+} (Ln=Tb, Eu, Dy) and V^{5+} Ion-Doped YPO_4 Nano-/Microstructures with Tunable Luminescent Colors, *Chem. Mater.*, 2009, **21**, 4598–4607.

4 Y. Zhuang, D. Chen, W. Chen, W. Zhang, X. Su, R. Deng, Z. An, H. Chen and R. J. Xie, X-ray-charged bright persistent luminescence in $NaYF_4$:Ln^{3+}@$NaYF_4$ nanoparticles for multidimensional optical information storage, *Light: Sci. Appl.*, 2021, **10**, 132.

5 Y. Xie, Y. Song, G. Sun, P. Hu, A. Bednarkiewicz and L. Sun, Lanthanide-doped heterostructured nanocomposites toward advanced optical anti-counterfeiting and information storage, *Light: Sci. Appl.*, 2022, **11**, 150.

6 D. Yu, H. Li, D. Zhang, Q. Zhang, A. Meijerink and M. Suta, One ion to catch them all: Targeted high-precision Boltzmann thermometry over a wide temperature range with Gd^{3+}, *Light: Sci. Appl.*, 2021, **10**, 236.

7 L. Qiu, P. Wang, J. Mao, Z. Liao, F. Chi, Y. Chen, X. Wei and M. Yin, Cr^{3+}-Doped $InTaO_4$ phosphor for multi-mode temperature sensing with high sensitivity in a physiological temperature range†, *Inorg. Chem. Front.*, 2022, **9**, 3187–3199.

8 C. Abram, B. Fond and F. Beyrau, Temperature measurement techniques for gas and liquid flows using thermographic phosphor tracer particles, *Prog. Energy Combust. Sci.*, 2018, **64**, 93–156.

9 Y. Hasegawa and Y. Kitagawa, Thermo-sensitive luminescence of lanthanide complexes, clusters, coordination polymers and metal–organic frameworks with organic photosensitizers, *J. Mater. Chem. C*, 2019, **7**, 7494–7511.

10 O. A. Savchuk, J. J. Carvajal, C. Cascales, J. Massons, M. Aguiló and F. Díaz, Thermochromic upconversion nanoparticles for visual temperature sensors with high thermal, spatial and temporal resolution, *J. Mater. Chem. C*, 2016, **4**, 6602–6613.

11 W. Qin, J. Ma, Y. Zhou, Q. Hu, Y. Zhou and G. Liang, Simultaneous promotion of efficiency and lifetime of organic phosphorescence for self-referenced temperature sensing, *Chem. Eng. J.*, 2020, **400**, 125934.

12 Z. Zheng, J. Zhang, X. Liu, R. Wei, F. Hu and H. Guo, Luminescence and self-referenced optical temperature sensing performance in $Ca_2YZr_2Al_3O_{12}$:Bi^{3+}, Eu^{3+} phosphors, *Ceram. Int.*, 2020, **46**, 6154–6159.

13 W. Ran, H. M. Noh, S. H. Park, B. R. Lee, J. H. Kim, J. H. Jeong and J. Shi, Er^{3+}-Activated $NaLaMgWO_6$ double perovskite phosphors and their bifunctional application in solid-state lighting and non-contact optical thermometry†, *Dalton Trans.*, 2019, **48**, 4405–4412.

14 M. Wu, D. Deng, F. Ruan, B. Chen and S. Xu, A spatial/temporal dual-mode optical thermometry based on double-sites dependent luminescence of $Li_4SrCa(SiO_4)_2$: Eu^{2+} phosphors with highly sensitive luminescent thermometer, *Chem. Eng. J.*, 2020, **396**, 125178.

15 J. Liao, M. Wang, F. Lin, Z. Han, B. Fu, D. Tu, X. Chen, B. Qiu and H. R. Wen, Thermally boosted upconversion and downshifting luminescence in $Sc_2(MoO_4)_3$: Yb/Er with two-dimensional negative thermal expansion, *Nat. Commun.*, 2022, **13**, 2090.

16 L. Ruan and Y. Zhang, Upconversion Perovskite Nanocrystal Heterostructures with Enhanced Luminescence and Stability by Lattice Matching, *ACS Appl. Mater. Interfaces*, 2021, **13**, 51362–51372.

17 M. Ding, B. Dong, Y. Lu, X. Yang, Y. Yuan, W. Bai, S. Wu, Z. Ji, C. Lu, K. Zhang and H. Zeng, Energy Manipulation in Lanthanide-Doped Core–Shell Nanoparticles for Tunable Dual-Mode Luminescence toward Advanced Anti-Counterfeiting, *Adv. Mater.*, 2020, **32**, 2002121.

18 J. Xue, X. Wang, J. H. Jeong and X. Yan, Fabrication, photoluminescence and applications of quantum dots embedded glass ceramics, *Chem. Eng. J.*, 2020, **383**, 123082.

19 A. G. Macedo, R. A. S. Ferreira, D. Ananias, M. S. Reis, V. S. Amaral, L. D. Carlos and J. Rocha, Effects of Phonon Confinement on Anomalous Thermalization, Energy Transfer, and Upconversion in Ln^{3+}-Doped Gd_2O_3 Nanotubes, *Adv. Funct. Mater.*, 2010, **20**, 624–634.

20 G. Gao, D. Busko, N. Katumo, R. Joseph, E. Madirov, A. Turshatov, I. A. Howard and B. S. Richards, Ratiometric Luminescent Thermometry with Excellent Sensitivity over a Broad Temperature Range Utilizing Thermally-Assisted and Multiphoton Upconversion in Triply-Doped La_2O_3:Yb^{3+}/Er^{3+} /Nd^{3+}, *Adv. Opt. Mater.*, 2021, **9**, 2001901.

21 M. Ni, W. Luo, D. Wang, Y. Zhang, H. Peng, X. Zhou and X. Xie, Orthogonal Reconstruction of Upconversion and Holographic Images for Anticounterfeiting Based on Energy Transfer, *ACS Appl. Mater. Interfaces*, 2021, **13**, 19159–19167.

22 P. Lei, P. Zhang, S. Yao, S. Song, L. Dong, X. Xu, X. Liu, K. Du, J. Feng and H. Zhang, Optimization of Bi^{3+} in Upconversion Nanoparticles Induced Simultaneous Enhancement of Near-Infrared Optical and X-ray Computed Tomography Imaging Capability, *ACS Appl. Mater. Interfaces*, 2016, **8**, 27490–27497.

23 L. Y. Wang, Y. Zhang and Y. Y. Zhu, One-pot synthesis and strong near-infrared upconversion luminescence of poly (acrylic acid)-functionalized YF_3:Yb^{3+}/Er^{3+} nanocrystals, *Nano Res.*, 2010, **3**, 317–325.

24 G. Xiang, J. Zhang, Z. Hao, X. Zhang, G.-H. Pan, L. Chen, Y. Luo, S. Lu and H. Zhao, Solvothermal synthesis and upconversion properties of about 10 nm orthorhombic LuF_3: Yb^{3+}, Er^{3+} rectangular nanocrystals, *J. Colloid Interface Sci.*, 2015, **459**, 224–229.

25 Y. Feng, Z. Li, Q. Li, J. Yuan, L. Tu, L. Ning and H. Zhang, Internal OH^- induced cascade quenching of upconversion luminescence in $NaYF_4$: Yb/Er nanocrystals, *Light: Sci. Appl.*, 2021, **10**, 105.

26 Y. Hua and J. S. Yu, Strong Green Emission of Erbium(III)-Activated La_2MgTiO_6 Phosphors for Solid-State Lighting and Optical Temperature Sensors, *ACS Sustainable Chem. Eng.*, 2021, **9**, 5105–5115.

27 X. Huang, B. Li and H. Guo, Synthesis, photoluminescence, cathodoluminescence, and thermal properties of novel Tb^{3+}-doped BiOCl green-emitting phosphors, *J. Alloys Compd.*, 2017, **695**, 2773–2780.

28 K. Li, H. Lian, M. Shang and J. Lin, A novel greenish yellow-orange red $Ba_3Y_4O_9$:Bi^{3+}, Eu^{3+} phosphor with efficient energy transfer for UV-LEDs, *Dalton Trans.*, 2015, **44**, 20542–20550.

29 J. C. Zhou, Z. L. Yang, W. Dong, R. J. Tang, L. D. Sun and C. H. Yan, Bioimaging and toxicity assessments of near-infrared upconversion luminescent $NaYF_4$:Yb,Tm nanocrystals, *Biomaterials*, 2011, **32**, 9059–9067.

30 X. Zhao, H. Suo, Z. Zhang and C. Guo, Upconverting CeO_2: Yb^{3+}/Tm^{3+} hollow nanospheres for photo-thermal sterilization and deep-tissue imaging in the first biological window, *Ceram. Int.*, 2019, **45**, 21910–21916.

31 H. X. Zhang, Y. Fan, P. Pei, C. X. Sun, L. F. Lu and F. Zhang, Tm^{3+}-Sensitized NIR-II Fluorescent Nanocrystals for In Vivo Information Storage and Decoding, *Angew. Chem., Int. Ed.*, 2019, **58**, 10153–10157.

32 K. Zhu, Z. Wang, H. Xu and Z. Fu, Development of Multifunctional Materials Based on Heavy Concentration Er^{3+}-Activated Lead-free Double Perovskite $Cs_2NaBiCl_6$, *Adv. Opt. Mater.*, 2022, **10**, 2201182.

33 H. Huang, S. Wang, R. Chen, N. Zhang, H.-R. Yao, Y. Zheng, F. Huang and D. Chen, Engineering upconverting core-shell nano-probe for spectral responsive fluid velocimetry, *Nano. Res.*, 2022, **16**, 1212–1219.

34 H. Suo, C. Guo, W. Wang, T. Li, C. Duan and M. Yin, Mechanism and stability of spectrally pure green up-conversion emission in Yb^{3+}/Ho^{3+} co-doped $Ba_5Gd_8Zn_4O_{21}$ phosphors, *Dalton Trans.*, 2016, **45**, 2629–2636.

35 S. Zhang, H. Liang, C. Liu, Z. Qi, T. Shao and Y. Wang, High color purity red-emission of NaGdTiO4:Pr^{3+} via quenching of $^3P_0$ emission under low-voltage cathode ray excitation, *Opt. Lett.*, 2013, **38**, 612–614.

36 I. Levin, T. A. Vanderah, T. G. Amos and J. E. Maslar, Structural Behavior and Raman Spectra of Perovskite-Like Solid Solutions (1−x) $LaMg_{0.5}Ti_{0.5}O_{3-x}La_{2/3}TiO_3$, *Chem. Mater.*, 2005, **17**, 3273–3280.

37 Y. Hua, W. Ran and J. S. Yu, Excellent photoluminescence and cathodoluminescence properties in Eu^{3+}-activated Sr_2LaNbO_6 materials for multifunctional applications, *Chem. Eng. J.*, 2021, **406**, 127154.

38 P. Dang, G. Li, X. Yun, Q. Zhang, D. Liu, H. Lian, M. Shang and J. Lin, Thermally stable and highly efficient red-emitting Eu^{3+}-doped $Cs_3GdGe_3O_9$ phosphors for WLEDs: non-concentration quenching and negative thermal expansion, *Light: Sci. Appl.*, 2021, **10**, 29.

39 S. Huang, L. Yu, K. Peng, Y. Zhao, J. Wang and M. Shang, Broadband excited $Na_3Tb(PO_4)_2$:Ce^{3+}/Eu^{2+} green/yellow–emitting phosphors with high color purity for LED–based application, *J. Am. Ceram. Soc.*, 2021, **104**, 5848–5858.

40 H. Lv, P. Du, W. Li and L. Luo, Tailoring of Upconversion Emission in Tm^{3+}/Yb^{3+}-Codoped $Y_2Mo_3O_{12}$ Submicron Particles Via Thermal Stimulation Engineering for Non-invasive Thermometry, *ACS Sustainable Chem. Eng.*, 2022, **10**, 2450–2460.

41 R. Hu, Y. Zhao, Y. Zhang, X. Wang, G. Li and M. Deng, Opto-mechano-thermo-sensitive allochroic luminescence based on coupled dual activators in tantalate towards multidimensional stimulus sensing, *Inorg. Chem. Front.*, 2023, **10**, 1225–1237.

42 Q. Liu, E. Pan, H. Deng, F. Liu and J. Li, Dy^{3+} doped (K,Na) NbO_3-based multifunctional ceramics for achieving enhanced temperature-stable piezoelectricity and non-contact optical temperature sensing performance, *Inorg. Chem. Front.*, 2023, **10**, 2359–2369.

43 L. Qiu, P. Wang, J. Mao, Z. Liao, F. Chi, Y. Chen, X. Wei and M. Yin, Cr^{3+}-Doped $InTaO_4$ phosphor for multi-mode temperature sensing with high sensitivity in a physiological temperature range, *Inorg. Chem. Front.*, 2022, **9**, 3187–3199.

44 Y. Tong, W. Zhang, R. Wei, L. Chen and H. Guo, $Na_2YMg_2(VO_4)_3$: Er^{3+}, Yb^{3+} phosphors: Up-conversion and optical thermometry, *Ceram. Int.*, 2021, **47**, 2600–2606.

45 S. F. León-Luis, U. R. Rodríguez-Mendoza, E. Lalla and V. Lavín, Temperature sensor based on the Er^{3+} green upconverted emission in a fluorotellurite glass, *Sens. Actuators, B*, 2011, **158**, 208–213.

46 H. Yu, W. Su, L. Chen, D. Deng and S. Xu, Excellent temperature sensing characteristics of europium ions self-reduction $Sr_3P_4O_{13}$ phosphors for ratiometric luminescence thermometer, *J. Alloys Compd.*, 2019, **806**, 833–840.

47 Z. Sun, Z. Fu, L. Ma, H. Cao, M. Wang, H. Cao and A. Zhang, Excellent multi-color emission and multi-mode optical ratiometric thermometer in (Ca, Tb, Eu, Sm)Nb_2O_6 phosphors based on wide O^{2-}→Nb^{5+} CTB, *Appl. Surf. Sci.*, 2022, **575**, 151791.

48 P. Du, J. Tang, W. Li and L. Luo, Exploiting the diverse photoluminescence behaviors of $NaLuF_4$:xEu^{3+} nanoparticles and g-C_3N_4 to realize versatile applications in white light-emitting diode and optical thermometer, *Chem. Eng. J.*, 2021, **406**, 127165.

49 M. Jia, Z. Sun, M. Zhang, H. Xu and Z. Fu, What determines the performance of lanthanide-based ratiometric nanothermometers?, *Nanoscale*, 2020, **12**, 20776–20785.

50 P. Du and J. S. Yu, Near-ultraviolet light induced visible emissions in Er^{3+}-activated La_2MoO_6 nanoparticles for

solid-state lighting and non-contact thermometry, *Chem. Eng. J.*, 2017, **327**, 109–119.

51 M. Jia, Z. Sun, F. Lin, B. Hou, X. Li, M. Zhang, H. Wang, Y. Xu and Z. Fu, Prediction of Thermal-Coupled Thermometric Performance of Er^{3+}, *J. Phys. Chem. Lett.*, 2019, **10**, 5786–5790.

52 L. Wu, M. Jia, D. Li and G. Chen, Shell Engineering on Thermal Sensitivity of Lifetime-Based NIR Nanothermometers for Accurate Temperature Measurement in Murine Internal Liver Organ, *Nano Lett.*, 2023, **23**, 2862–2869.

53 J. Zhang, Y. Zhang and X. Jiang, Investigations on upconversion luminescence of $K_3Y(PO_4)_2$: Yb^{3+}-Er^{3+}/Ho^{3+}/Tm^{3+} phosphors for optical temperature sensing, *J. Alloys Compd.*, 2018, **748**, 438–445.

54 X. Wang, X. Li, S. Xu, L. Cheng, J. Sun, J. Zhang and B. Chen, Can temperature be accurately sensed by red-green emission ratio in $YNbO_4$: Ho^{3+}/Yb^{3+} phosphor under 980 nm excitation?, *J. Alloys Compd.*, 2018, **754**, 222–226.

55 M. Jia, F. Lin, Z. Sun and Z. Fu, Novel excited-state nanothermometry combining the red-shift of charge-transfer bands and a thermal coupling effect†, *Inorg. Chem. Front.*, 2020, **7**, 3932–3937.

56 C. D. S. Brites, S. Balabhadra and L. D. Carlos, Lanthanide-Based Thermometers: At the Cutting-Edge of Luminescence Thermometry, *Adv. Opt. Mater.*, 2019, **7**, 1801239.